Università degli Studi di Trieste
Archivio della ricerca – postprint

Photoabsorption of Icosahedral Noble Metal Clusters: An Efficient TDDFT Approach to Large-Scale Systems

Oscar Baseggio, Martina De Vetta, Giovanna Fronzoni, and Mauro Stener*

Dipartimento di Scienze Chimiche e Farmaceutiche, Università di Trieste, Via Giorgieri 1, 34127 Trieste, Italy

Luca Sementa and Alessandro Fortunelli*

CNR-ICCOM, Consiglio Nazionale delle Ricerche, via Giuseppe Moruzzi 1, 56124 Pisa, Italy

Arrigo Calzolari*

CNR-NANO, Istituto Nanoscienze, Centro S3 Via Campi 213/A, I-41125 Modena, Italy

Supporting Information

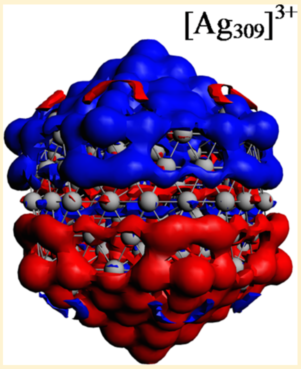

ABSTRACT: We apply a recently developed time-dependent density functional theory (TDDFT) algorithm based on the complex dynamical polarizability to calculate the photoabsorption spectrum of the following series of closed-shell icosahedral clusters of increasing size (namely, $[M_{13}]^{5+}$, $[M_{55}]^{3-}$, $[M_{147}]^{-}$, and $[M_{309}]^{3+}$ with M = Ag, Au), focusing in particular on their plasmonic response. The new method is shown to be computationally very efficient: it simultaneously retains information on the excited-state wave function and provides a detailed analysis of the optical resonances, e.g., by employing the transition contribution map scheme. For silver clusters, a very intense plasmon resonance is found for $[Ag_{55}]^{3-}$, with strong coupling among low-energy single-particle configurations. At variance, for gold clusters we do not find a single strong plasmonic peak but rather many features of comparable intensity, with partial plasmonic behavior present only for the lowest-energy transitions. Notably, we also find a much greater sensitivity of the optical response of Ag clusters with respect to Au clusters to cluster charge, the exchange-correlation (xc) functional, and the basis set, as demonstrated via a detailed comparison between $[Ag_{55}]^q$ and $[Au_{55}]^q$. The results of the TDDFT algorithm obtained with the complex dynamical polarizability are finally compared with those produced by alternative (real-time evolution or Lanczos) approaches, showing that, upon proper choice of numerical parameters, overall nearly quantitative agreement is achieved among all of the considered approaches, in keeping with their fundamental equivalence.

1. INTRODUCTION

The calculation of photoabsorption spectra for large molecules is nowadays considered to be a standard task in quantum chemistry, and this has become possible thanks to the accuracy of the time-dependent density functional theory (TDDFT) formalism, which includes most of the physics of linear optical response phenomenon as well as its efficient implementation in publicly available quantum chemistry codes.

The most common way to tackle this problem in quantum chemistry consists first of solving the Kohn–Sham (KS) equations of density functional theory (DFT) by expanding the molecular KS orbitals as linear combinations of atomic functions and second of recasting the TDDFT equations in a form involving the diagonalization of matrix Ω according to the density matrix formulation of Casida.[1] In this scheme, the TDDFT problem is reduced to the extraction of the eigenvalues and eigenvectors of Ω, a matrix whose dimension is the product of the number of occupied and virtual orbitals ($N_{occ} \times N_{virt}$), which can thus be huge for large systems. Such an approach has been implemented in many codes, such as ADF,[2−4] and can be made efficient by taking advantages of (a) the point group molecular symmetry, (b) the Davidson diagonalization iterative algorithm that is well suited for very large matrices, (c) electron density fitting techniques through the use of auxiliary basis functions, and finally (d) massive parallelization. This scheme can be computationally feasible even for very large molecules (up to hundreds of atoms) provided one is interested only in the lowest part of the absorption spectrum. However, because of the intrinsic limitation of the Davidson algorithm, which becomes numerically unstable when too many eigenvalues are requested, the higher-energy part of the spectrum of large molecules is basically inaccessible. This situation is encountered, for example, in the calculation of the photoabsorption spectra of metal clusters that exhibit plasmonic behavior because the clusters are quite large and the plasmons lie at moderately high energy so that the number of eigenvalues requested is potentially too high to be practicable using the Davidson algorithm. For this reason, alternative approaches, based on, for example, the real-time propagation of the wave function[5] or on Lanczos chains,[6] have been considered as possible alternatives to the Casida scheme. The schemes developed by Grimme consisting of simplified TDA[7] and TDDFT[8] are also worth mentioning, and a linear-scaling TDDFT algorithm has been proposed by Zuehlsdorff.[9] Very recently, Nobusada developed a massively parallel implementation of TDDFT based on real time and real space.[10] The real-time approach developed by Govind[11] and the spin-adapted one developed by Li[12] represent other important contributions to the field.

The real-time schemes do not suffer from energy limitation issues in the calculation of the spectrum but partially lose information for the excited-state wave function so that very useful analysis tools that are naturally included in the Casida scheme become less straightforward. Such an analysis allows one to describe electron excitations as a linear combination of one-electron excited configurations and therefore gives a complete description of the photoabsorption spectrum in terms of electronic structure. To avoid the diagonalization bottleneck and simultaneously keep the useful analysis of excitations, recently a new TDDFT algorithm has been proposed[13] that extracts the spectrum from the calculation of the complex dynamical polarizability. In this approach, the TDDFT equations are projected onto the density fitting auxiliary basis set and therefore the associated numerical problem is recast into the resolution of a nonhomogeneous linear system with a dimension much smaller with respect to that of the Casida approach. The matrix dimension of such linear system is $k \times (N_{\mathrm{occ}} + N_{\mathrm{virt}})$ instead of $N_{\mathrm{occ}} \times N_{\mathrm{virt}}$ of the Casida Ω matrix, with $k = 1.91$ or 1.6 for Au and Ag, respectively. In this new scheme, the spectrum at each frequency is obtained as an independent calculation; moreover, the algorithm is easily parallelizable and applicable essentially to all systems for which a DFT calculation is affordable. The potentials of this approach are demonstrated in the present work by studying two series of noble metal clusters (Ag and Au) containing up to 309 atoms. Noble metal clusters are systems of great interest because they play an important role in many different fields, for example, catalysis and material science. More specifically their optical properties deserve special attention in terms of both basic science and technological applications (optoelectronic devices, thermal treatment of cancer, cell imaging, i.e., colorimetric probes for DNA detection, realization of nanoantennas, application in SERS spectroscopy, etc.).[14−16] In fact, noble metal nanoparticles exhibit surface plasmonic resonance (SPR), a very intense optical absorption peak in the UV−vis region, due to the coherent and collective oscillation of the metal free electrons subjected to electromagnetic radiation. Fundamental open issues exist in this field, for example, the dependence of the shape and peak of SPR on the nanoparticle size and shape. From a more theoretical and computational point of view, the formalism to describe the SPR must go beyond the one-electron description as a result of the collective nature of the SPR but must also be very efficient because the SPR shows up when the cluster size goes beyond at least 2 nm. For these reasons, a very efficient TDDFT algorithm should be, at the moment, the most promising way to study plasmonics in nanoclusters theoretically.

It is first shown that the new algorithm is very efficient, especially for the larger clusters that could not be treated by means of the standard Casida approach. For example, in $[\mathrm{Au}_{309}]^{3+}$ the dimension of the linear system in the present approach is only 13 596, whereas the dimension of the Casida Ω matrix would have been around 12 million. Finally, to validate the new approach and to firmly assess the equivalence of different TDDFT schemes, the photoabsorption spectra of Ag_{55} and Au_{55} clusters are also predicted and compared by using CP2K[17] and turboTDDFT codes,[18] which rely on real-time propagation of the wave function and Lanczos chain approaches, respectively. Interestingly, a comparison between the optical response of Ag and Au clusters shows a greater sensitivity of the Ag optical response to both physical and numerical parameters such as the charge state, the exchange-correlation (xc) functional, and the basis set, as a result of the intrinsically stronger free-electron character of Ag and the absence of strong s/d coupling with respect to Au.

The availability of an efficient method to treat photoabsorption in large systems opens the way to study the behavior of surface plasmon resonance (SPR), a typical optical property of noble metal nanoclusters with many potential applications.

2. THEORETICAL METHOD

The theoretical method and its implementation have been described in detail previously,[13] so here we give only a brief description of the salient features and refer the reader to the original work for more information about the algorithm and how to calculate the corresponding matrix elements.

The photoabsorption spectrum $\sigma(\omega)$ is calculated for each value of the photon energy ω from the imaginary part of the isotropic dynamical polarizability $\sigma(\omega)$:

$$\sigma(\omega) = \frac{4\pi\omega}{c}\mathrm{Im}[\alpha(\omega)] \tag{1}$$

The isotropic dynamical polarizability is calculated for a complex frequency, i.e., $\omega = \omega_r + i\omega_i$, where the real part ω_r corresponds to the actual photon frequency (energy) and ω_i is the imaginary part that refers to a broadening of the discrete lines and is interpreted as the excited-state finite lifetime.[19] For the calculation of the spectrum, the isotropic part of the tensor is actually extracted from its trace

$$\alpha(\omega) = \frac{1}{3}\sum_{i=1}^{3}\alpha_{ii}(\omega)$$

where index i runs on the three spatial components x, y, and z. The polarizability tensor is obtained from the following expression

$$\alpha_{zz}(\omega) = \int \rho_z^{(1)}(\omega, \overline{r}) z \, d\overline{r} \tag{2}$$

where $\rho_z^{(1)}(\omega, \overline{r})$ is the Fourier component of the given frequency of the first-order time-dependent density induced by the external time-dependent scalar potential and $\overline{r}$ represents the position vector whose components are the three coordinates x, y, and z. According to TDDFT, the induced density can be obtained from the dielectric susceptibility $\chi_{\mathrm{KS}}(\omega, \overline{r}, \overline{r}')$ of a reference system of noninteracting electrons under the effect of an effective potential $V_{\mathrm{SCF}}^{z}(\omega, \overline{r})$, which is the sum of the external potential plus the Coulomb and the response xc potentials. The explicit expression of the dielectric susceptibility can be found in ref 20.

This is summarized by the following coupled linear equations:

$$\rho_z^{(1)}(\omega, \bar{r}) = \int \chi_{\mathrm{KS}}(\omega, \bar{r}, \bar{r}')\, V_{\mathrm{SCF}}^z(\omega, \bar{r}')\, \mathrm{d}\bar{r}' \tag{3}$$

$$V_{\mathrm{SCF}}^z(\omega, \bar{r}) = V_{\mathrm{EXT}}^z(\omega, \bar{r}) + \int \frac{\rho_z^{(1)}(\omega, \bar{r}')\, \mathrm{d}\bar{r}'}{|\bar{r} - \bar{r}'|} + \left.\frac{\partial V_{\mathrm{XC}}}{\partial \rho}\right|_{\rho^{(0)}} \rho_z^{(1)}(\omega, \bar{r}) \tag{4}$$

The adiabatic local density approximation (ALDA)[20] is assumed in eq 4, and $V_{\mathrm{EXT}}^z(\omega, \bar{r})$ corresponds in practice to the z dipole component. Now eqs 3 and 4 can be written in operatorial form

$$\rho_z^{(1)} = \chi_{\mathrm{KS}} V_{\mathrm{SCF}}^z \tag{5}$$

$$V_{\mathrm{SCF}}^z = V_{\mathrm{EXT}}^z + K\rho_z^{(1)} \tag{6}$$

where in eq 6 K stands for the sum of the Coulomb and the xc kernels.

Because of the linearity of eqs 5 and 6, it is possible to eliminate V_{SCF}^z and to obtain an equation for $\rho_z^{(1)}$ that reads

$$[1 - \chi_{\mathrm{KS}} K]\rho_z^{(1)} = \chi_{\mathrm{KS}} V_{\mathrm{EXT}}^z \tag{7}$$

Equation 7 is then represented over the basis set of the auxiliary density fitting functions f_μ. More precisely, only a subset of the fitting set is enough to obtain convergent results. Within this representation, the induced density assumes the expression

$$\rho_z^{(1)}(\omega, \vec{r}) = \sum_{\mu}^{K} f_\mu(\bar{r})\, b_\mu(\omega)$$

and the following nonhomogeneous system of linear algebraic equations can be written in matrix formulation form:

$$[\mathbf{S} - \mathbf{M}(\omega)]\mathbf{b} = \mathbf{d} \tag{8}$$

In eq 8, **S** is the overlap matrix between fitting functions, **b** is the unknown vector with expansion coefficients $b_\mu(\omega)$ of $\rho_z^{(1)}$, **d** is the frequency-dependent vector corresponding to the known nonhomogeneous term whose components are

$$d_\mu = \langle f_\mu | \chi_{\mathrm{KS}}(\omega) | z \rangle \tag{9}$$

and finally the elements of frequency-dependent matrix **M** are

$$M_{\mu\nu} = \langle f_\mu | \chi_{\mathrm{KS}}(\omega) K | f_\nu \rangle \tag{10}$$

In practice, eq 8 is solved for each value of the photon energy.

It is important to recall that present TDDFT implementation should be employed only below the ionization threshold. This limitation is due to the localized nature of the basis set (STO), which is suited for describing the long-range behavior in real space of the bound states only.

For comparison, in the case of the $[\mathrm{Ag}_{55}]^{5+}$ and $[\mathrm{Au}_{55}]^{5+}$ clusters the photoabsorption spectrum has been calculated with CP2K and QE codes as well.

In the CP2K code,[17] the time-dependent Kohn−Sham (TDKS) equations are explicitly integrated in time (see next section for computational details), and from the so-produced time-resolved TDKS solution, the TDDFT spectrum is obtained via Fourier transform of the time-dependent dipole moment resulting from a small instantaneous electric field perturbation of the system wave function.

Within the QE suite of programs, the turbo TDDFT package[6,21] calculates the frequency-dependent polarizability as the trace of the product between the dipole operator and the response density matrix, where the latter is expressed as the solution of the linearized quantum Liouville equation. The specific Lanczos implementation does not require the explicit evaluation of empty (virtual) states, thus reducing the computational cost and allowing for the calculation of extended portions of the spectrum in systems comprising several hundred atoms.

3. COMPUTATIONAL DETAILS

The complex polarizability method has been implemented in a local version of the ADF code. The LB94[22] or the PBE[23] exchange-correlation xc functionals were employed to obtain the KS orbitals and eigenvalues from the KS equations, and the exchange-correlation kernel is approximated by ALDA[20] in the TDDFT part by taking the derivative of the VWN[24] LDA xc potential. The basis sets as well as the auxiliary density fitting functions employed consist of Slater type orbitals (STO) included in the ADF database. The new program uses a subset of the ADF fitting functions in order to save computer time by ignoring fitting functions that are not necessary for an accurate description of the photoabsorption spectrum. The choice of this subset was made via preliminary test calculations on Ag_2 and Au_2. The calculations have been performed at the scalar relativistic level with the zeroth-order relativistic approximation (ZORA).[25]

To give a quantitative idea of the computational efforts and the efficiency of the spectrum calculation from the complex polarizability, for $[\mathrm{Au}_{309}]^{3+}$ the SCF procedure was employed for 10 h using 16 cores on a Linux Infiniband Cluster with 8-core Intel Haswell 2.40 GHz processors, and the resolution of the TDDFT inhomogeneous linear system (dim = 13 596) employed only 145 s using 16 cores for each energy point. Because about 100 energy points are enough for a complete description of the spectrum, the TDDFT linear system resolution is comparable to the SCF effort. In addition, the matrix elements calculation time should also be considered, so in general a TDDFT calculation will be roughly comparable to a gradient calculation in terms of computational cost.

In the CP2K package,[17] a DVZP basis set[26] and GTH pseudopotentials[27] were employed in the calculations, with a real-space grid spacing of 0.25 Å. The PBE xc functional was used in the KS equations and dynamics. Starting from a ground-state calculation, an optical response is obtained by subjecting the system to electrical pulses (with a strength of 0.0005 a.u.) in each of the three Cartesian directions and using the time-evolution formalism to follow the electron dynamics. In total, we sampled 19.3 fs using a time step of 0.012 fs. Time damping of 7.3 fs was chosen to broaden the predicted spectrum.

The TurboTDDFT code is part of the Quantum-ESPRESSO (QE) package[18] for the simulation of the ground and excited states of solid-state systems based on (TD)DFT approaches. In the present case, the $[\mathrm{Ag}_{55}]^{5+}$ and $[\mathrm{Au}_{55}]^{5+}$ clusters have been simulated by using periodically repeated supercells, each including the metallic cluster (i.e., 55 atoms) and a thick layer of vacuum (∼18 Å) in the three spatial directions in order to avoid spurious interactions between adjacent replicas. The

PBE xc functional was used in solution of both DFT and TDDFT problems. The single-particle wave functions (charge) were expanded in plane waves up to an energy cutoff of 25 Ry (250 Ry). Atomic potentials were described by using ab initio ultrasoft pseudopotentials of the Vanderbilt type.[28] The 4d (5d) electrons of Ag (Au) have been explicitly included in the valence shell. The Brillouin zone of the reciprocal lattice was sampled at the Γ point. A jellium background is inserted to remove divergences in the charged cells, and the Martyna−Tuckerman correction[29] to both the total energy and self-consistent potential is applied to consider the system as isolated. Optical spectra were obtained by evaluating 10 000 Lanczos cycles for each incoming light polarization and then averaged over the three spatial directions.

4. RESULTS AND DISCUSSION

The behavior of surface plasmon resonance (SPR), a typical optical property of noble metal nanoclusters, has been the subject of many studies. SPR starts to appear in systems whose size is beyond about 2 nm, therefore containing more than 150−200 atoms. The size and shape effects are quite important factors that have a strong influence on the energy position and the intensity of the SPR. Shape can also be profitably exploited to study SPR behavior in systems that are elongated in only one dimension (nanowires), thus enabling a plasmonlike optical response in clusters containing less than 100 atoms.[30] Small noble metal clusters do not arrange in the bulk fcc structure because surface tension effects tend to destabilize such configurations. Instead, they prefer to assume more spherical shapes, such as icosahedral or decahedral. In this work, we have considered only the most symmetric icosahedral structures.

Contrary to bulk systems, where plasmons can be excited only by a longitudinal external electric field, in the case of nanoparticles and clusters SPRs can be excited also by transversal incoming fields, i.e., light. Thus, plasmonic features of nanostructures can be easily characterized starting from their optical absorption spectra. Several previous TDDFT studies are available for both silver and gold nanoclusters,[31−39] but more specific works on icosahedral noble metal cluster series are available for silver up to Ag_{55}[40] and Ag_{561}[41] and for gold up to Au_{55}[42] and Au_{1414}[43] atoms. Moreover, a very recent real-time TDDFT investigation on the icosahedral Ag_{55} cluster addressed the specific interplay between plasmon and single-particle excitations.[44] Unfortunately, in these studies different methods have been employed to treat the largest systems with respect to the smaller ones in terms of both the exchange-correlation functional and the numerical implementation (Casida-like or real-time propagation) so that a precise assessment of size-dependence effects is not readily available. The present work consists, instead, of a fully coherent study of metal clusters of both Ag and Au by using the same method and the same level of accuracy for all considered sizes. This investigation is also supplemented with an analysis of the electron transitions in terms of one-electron excited configurations, which will be conveniently presented in graphical compact form according to the bidimensional transition contribution map (TCM) plots.[45]

4.1. Cluster Geometry. The icosahedral clusters have been built starting with the simple M_{13} system, adding further shells according to a Mackay protocol. The cluster structure has not been optimized but is kept fixed by imposing that the average interatomic distance is equal to the experimental bulk value; indeed, it has been shown that structural relaxation has only a minor impact on the optical properties of gold clusters.[46] In the regular icosahedron, two different interatomic distances are defined, the intershell (R) and the intrashell (D) ones, which are connected by the following geometric relation: $\frac{R}{D} = \sqrt{\frac{5+\sqrt{5}}{8}}$. Therefore, we have taken $\frac{R+D}{2}$ to be equal to 2.89 and 2.88 Å for Ag and Au clusters, respectively.

4.2. Photoabsorption of the $[Ag_n]^q$ Series. We have considered the first four members of the series of icosahedral silver clusters $[Ag_{13}]^{5+}$, $[Ag_{55}]^{3-}$, $[Ag_{147}]^{-}$, and $[Ag_{309}]^{3+}$. The charges have been chosen in order to have a closed-shell electronic structure because the complex polarizability method at the moment cannot treat open shells.

The photoabsorption spectra of this series, calculated at the complex polarizability TDDFT level with the LB94[22] xc functional and DZ basis set, are reported in Figure 1. Apart from the smallest cluster $[Ag_{13}]^{5+}$, all of the others are characterized by a very strong peak that grows and is red-shifted with increasing cluster size, a behavior that is typical of plasmon resonance.[47] In $[Ag_{55}]^{3-}$, the peak is actually split in two very close contributions. The energy of the maxima are at 4.70, 4.30, and 3.95 eV for $[Ag_{55}]^{3-}$, $[Ag_{147}]^{-}$, and $[Ag_{309}]^{3+}$, respectively, so it seems that the energy of the plasmon resonance is still decreasing and has not yet reached its limiting value. It is interesting to compare this finding with a previous TDDFT study[41] on the same icosahedral silver clusters that had employed a very accurate real-time propagation method and the adiabatic GLLBSC potential.[48,49] In such a study, all of the peaks were calculated at lower energies with respect to the present work by 0.5−0.2 eV, and more interestingly, a red shift of 0.4 eV was actually found on going from Ag_{55} to Ag_{147}, which is in good agreement with the present calculation, whereas a very small red shift of only 0.1 eV was found on going from Ag_{147} to Ag_{309}. The difference in the energy of the maxima between the two calculations is not surprising and can be assigned to the different xc functionals employed. In the previous work,[41] the energy position of the resonance for Ag_{147} calculated with the PBE functional was found at about 3.2 eV, i.e., shifted by 0.6 eV with respect to the value calculated at the GLLBSC level (3.8 eV). The calculated spectrum of $[Ag_{55}]^{3-}$ is in good agreement with that calculated by ADF with the DZ basis set and the LB94 xc functional reported in ref 40, showing the same double peak shape, although the present spectrum is shifted by about 0.1−0.2 eV to higher energy. To check this point, we have calculated the spectrum (not shown) for

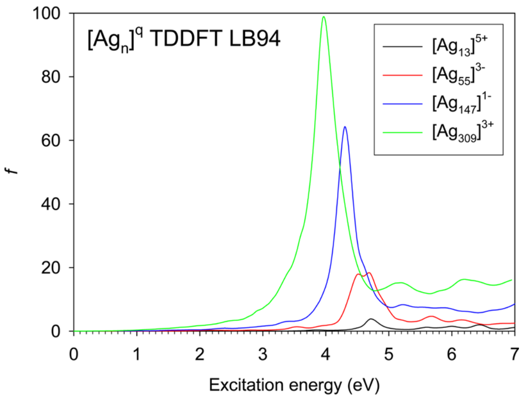

Figure 1. Photoabsorption profiles of $[Ag_{13}]^{5+}$, $[Ag_{55}]^{3-}$, $[Ag_{147}]^{-}$, and $[Ag_{309}]^{3+}$ calculated by complex polarizability TDDFT DZ LB94. Imaginary broadening ω_i = 0.15 eV.

$[Ag_{55}]^{3-}$ with the ADF program employing the Casida approach with the geometry of the present work and have obtained perfect agreement with the results produced by the complex polarizability algorithm reported in Figure 1. We can conclude that three possible causes of this discrepancy can be considered: the basis set, the xc functional, and the cluster geometry, which in ref 40 was relaxed in C_{5v} symmetry.

Besides a strong plasmonic resonance, the calculated spectra do not show other important features, and only a weak intensity modulation is apparent for all of the clusters above 5 eV. Although in this case the plasmonic behavior is clear cut, in general it is very difficult to distinguish between a molecular-like resonance and a plasmon: a general analysis has been suggested by Jacob et al.[50] but requires recalculation of the spectra many times with different values of coupling parameter λ, so such a procedure can be impractical for very large systems such as the present ones. For this reason, in order to gain better insight into the physics that governs the plasmonic features in metal clusters, here we have performed a TCM analysis[45] of the spectrum, in correspondence with the maximum in the intensity as reported in Figure 2. The TCM plots are very convenient 2D representations of the one-electron excited configuration coefficients that contribute to the excited state: each excited determinant corresponds to a point in the plane, the value on the X axis corresponds to the occupied orbital energy, and the value on the Y axis corresponds to the unoccupied orbital energy. For each excited determinant, a 2D Gaussian function is added, with a weight proportional to its coefficient in the excited-state expansion.

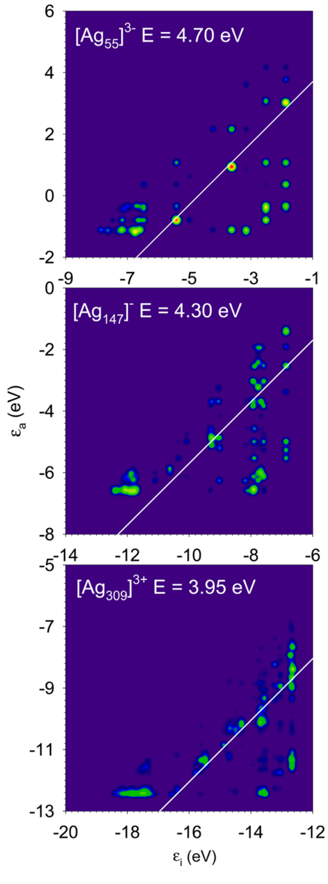

Figure 2. TCM plots for $[Ag_{55}]^{3-}$, $[Ag_{147}]^{-}$, and $[Ag_{309}]^{3+}$ taken at plasmon energies E. ε_i (X axis) and ε_a (Y axis) refer to occupied and virtual orbital energies. Each white line corresponds to $\varepsilon_a - \varepsilon_i = E$.

Before we start the discussion, it is useful to recall the typical nature of plasmons in Ag and Au clusters. In silver, the plasmon consists of a collective intraband sp → sp transition, and in gold, it is mixed with interband d → sp transitions: this mixing screens the plasmon so that in gold it is less intense than in silver, at least when the cluster size is still small, as in the present study.

We start the analysis with the $[Ag_{55}]^{3-}$ plasmon at 4.70 eV (upper panel in Figure 2); in the TCM plot, we have also added a white line that corresponds to the unoccupied−occupied orbital eigenvalue difference equal to the excitation energy. To read the TCM plots properly, it must be remembered that for Ag clusters the sp band covers all occupied and unoccupied orbitals and the d band is confined to well below the Fermi level (ε_F), as reported in the DOS plots in Figure 3 of ref 41. In the present case, the upper limit of the d band is at −6.2 eV (X axis), which is about 4.7 eV below ε_F. Therefore, in the TCM plot of $[Ag_{55}]^{3-}$ all of the spots correspond to intraband sp → sp configurations, with the only exception being the region around −7 eV on the X axis that instead corresponds to interband d → sp configurations. Therefore, the plasmon consists essentially of an intraband sp → sp excitation. The collective nature of the plasmon can be inferred by the presence of many spots in the TCM. Moreover, it is worth noting that three strong spots lie on the white line, which correspond to electron promotion between orbitals whose energy difference matches the plasmon energy almost exactly. On the other hand, there are important contributions coming from configurations having energies well below the plasmon, in particular, between −4 and −2 eV in the occupied orbitals (X axis) and between −1 and 1 eV in the virtual orbitals (Y axis). On the contrary, the configurations having energies above the plasmon excitation play only a minor role: the only important contribution comes from the already-identified interband d → sp configurations, along with a few weak ones coming from the sp → sp at around 2 to 3 eV in the virtual orbitals (Y axis). It is important to discriminate the contributions according to their energy: the presence of contributions with an eigenvalue energy difference that is different with respect to the plasmon resonance indicates a strong coupling among them. On the other hand, if the eigenvalue energy difference matches the plasmon energy, then the contributions are almost degenerate with the plasmon but not necessarily coupled to it. The fundamental role played by low-energy transitions in plasmons has been pointed out in a previous study[51] that employed model configuration interaction (CI) calculations.

The TCM plots for the plasmons of $[Ag_{147}]^{-}$ and $[Ag_{309}]^{3+}$ at 4.30 and 3.95 eV, respectively, are also reported in Figure 2, displaying very similar patterns as in $[Ag_{55}]^{3-}$. In both cases, the interband d → sp "island" is observed at ca. −12 eV in $[Ag_{147}]^{-}$ and at ca. −18 eV in $[Ag_{309}]^{3+}$ in the occupied orbital energy scale. All other contributions pertain to the sp → sp intraband transitions. There are several contributions along the white line, indicating quasi-degeneracy between the excited configurations and the plasmon. Also in this case, important contributions from lower-energy configurations suggest strong configuration coupling and therefore collective behavior. By comparing the present TCM analysis with the previous one on the Au_{86} gold nanowire[30] and $[Au_{147}]^{-}$ icosahedral clusters,[13] we notice that the Au_{86} gold nanowire displayed a very strong plasmon peak and the most intense TCM contributions derived from lower-energy configurations, indicating strong configuration coupling. On the other hand, in the $[Au_{147}]^-$ cluster the plasmon peak was much weaker, and only minor contributions were found from low-energy configurations. All of this is consistent with the present analysis. The importance of the lower-energy contributions in plasmons has been pointed out in a previous real-time TDDFT study[44] and has proven fundamental to discriminate between plasmon and single-particle excitations.

In addition to the TCM analysis, we have also inspected the resonant part of the first-order time-dependent perturbed density, that is, the imaginary part of the solution of previous eq 7, calculated at the plasmon energy for the three largest silver clusters. The results are reported in Figure S1 of the Supporting Information. As expected, all of the plots display typical dipolar character consistent with the classical interpretation of the SPR in terms of charge density oscillations. This confirms the plasmonic nature of the resonance given above. However, it is worth noticing that it is not possible to extract from the simple perturbed density plots the same amount of information derived from the TMC plots that are confirmed to be a more powerful analysis tool.

4.3. Photoabsorption of the $[Au_n]^q$ Series.

In parallel with the silver clusters, we have considered an analogous series of icosahedral gold clusters $[Au_{13}]^{5+}$, $[Au_{55}]^{3-}$, $[Au_{147}]^-$, and $[Au_{309}]^{3+}$, with the same charge states as in the silver case so as to obtain a closed-shell electronic structure for all four clusters. The photoabsorption spectra of the cluster series, calculated at the TDDFT level with the LB94[22] xc functional and the DZ basis set, are reported in Figure 3. The spectra look very different with respect to silver: there is no leading peak that may be easily attributed to a plasmon resonance but rather a smoothly growing intensity starting at around 2−3 eV depending on the cluster, followed by a wide modulation displaying maxima at 3.50, 4.40, and 5.50 eV for $[Au_{309}]^{3+}$ and 3.50, 4.10, and 5.50 eV for $[Au_{147}]^-$. For the three largest gold clusters, the intensity is still growing up to 7 eV, and the absolute intensity is much weaker than for a silver cluster by a factor of 3. The absence of strong plasmons is not surprising: in a previous work on gold nanowires[30] it has been shown that a clear plasmon emerges only when the cluster size exceeds 2 nm. In the case of Au_{68} with a length of 2.02 nm, only an incipient weak plasmon was observed, whereas for Au_{86} with a length of 2.59 nm, a very intense plasmon was found. In the present work, the distances between the two most distant atoms of $[Au_{309}]^{3+}$ and $[Au_{147}]^-$ are 2.25 and 1.68 nm, respectively, so only a weak plasmon should be expected even for the largest cluster. It is worth noting that the $[Au_{147}]^-$ cluster has been considered as well in a previous work,[46] exhibiting a first plasmonic peak at 2.95 eV that is consistent with a shoulder found in the present work at around 3 eV. In that work, it was not possible to go beyond 3.2 eV because the Davidson algorithm implemented in ADF was not practical for extracting a larger number of eigenvalues. Interestingly, the absorption profile of the $[Au_{309}]^{3+}$ cluster also displays a shoulder at around 3.2 eV, which is very likely the evolution of the shoulder of $[Au_{147}]^-$ at 3 eV.

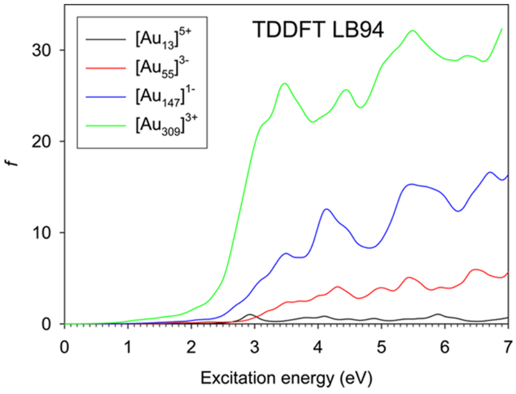

Figure 3. Photoabsorption profiles of $[Au_{13}]^{5+}$, $[Au_{55}]^{3-}$, $[Au_{147}]^-$, and $[Au_{309}]^{3+}$ calculated by complex polarizability TDDFT DZ LB94. Imaginary broadening ω_i = 0.15 eV.

To identify possible plasmonic behaviors, in Figure 4 we have considered the TCM analysis of the three most intense features of $[Au_{147}]^-$ and $[Au_{309}]^{3+}$. We start with $[Au_{147}]^-$ at 3.50 eV: taking into account (i) that the Au 5d band lies between −10 and −12 eV on the occupied orbital energy scale (*X* axis) and (ii) that the remaining states belong to the 6s6p band, we find that the leading contribution is a d → sp interband transition, with important intraband sp → sp contributions even from lower energies. This suggests that coupling is present and indicates a collective behavior typical of plasmons, at least to some extent. Going to the next maximum at 4.10 eV, we notice a drastic decrease in the role played by the lower-energy configurations and a concomitant increase in the d → sp interband transition character, so in this case the plasmonic

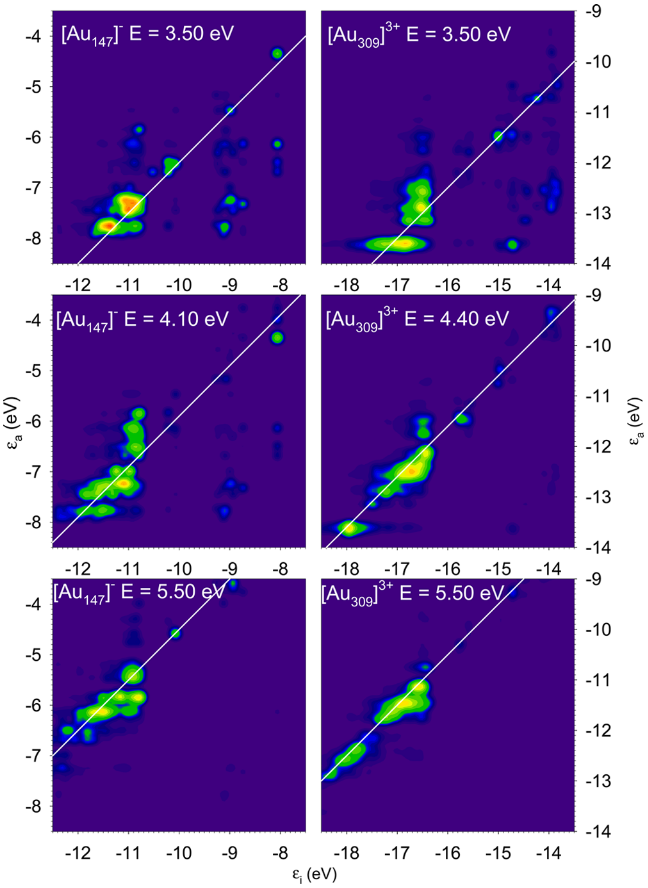

Figure 4. TCM plots for $[Au_{147}]^-$ and $[Au_{309}]^{3+}$ taken at energies corresponding to photoabsorption maxima *E*. ε_i (*X* axis) and ε_a (*Y* axis) refer to occupied and virtual orbital energies, respectively. Each white line corresponds to $\varepsilon_a - \varepsilon_i = E$.

behavior has almost disappeared. Finally, at 5.50 eV the coupling is negligible, so this feature does not carry any plasmonic character and can be classified as a pure d → sp interband transition.

Moving to the next cluster $[Au_{309}]^{3+}$ at 3.50 eV, we find again clear coupling with lower-energy configurations, confirming the plasmonic nature of this feature. The next peak at 4.40 eV displays only very weak coupling that disappears completely at 5.50 eV. We can summarize all of these findings by saying that the feature at 3.50 eV in both clusters has definite plasmonic-like nature, which is not pure but hybridized with d → sp interband excitations. Such hybridization is present also in the feature at 4.10 eV of $[Au_{147}]^{-}$. We can expect that as the cluster size increases this hybridization should decrease, giving rise to a strong, pure plasmon contribution at low energy followed by pure d → sp interband excitations at higher energy.

Moreover, we have considered the induced density, reported in Figure S2 of the Supporting Information. As in the previous case, all of them display the typical dipolar shape, consistent with the plasmon. The only noteworthy feature in the perturbed density is a kind of fringe that reduces the dipolar distribution of the density, well apparent in the equatorial faces of $[Au_{309}]^{3+}$ at 4.4 and 5.5 eV and to some extent in $[Au_{147}]^{-}$ at 5.5 eV. They might be an indication of reduced or absent plasmon character. Also, in this case the TCM analysis has provided much more informative than the induced density in assessing the nature of the spectral features in terms of the electronic structure.

4.4. Analysis of Photoabsorption for $[Ag_{55}]^q$.

Among the series of silver clusters, we have selected Ag_{55} as an example of a relatively small cluster to be further analyzed with other methods and with different schemes in order to assess the importance of the various computational approaches. In Figure 5, we consider the effect of the charge and of the xc functional. In the upper panel of Figure 5, the photoabsorption is calculated with the LB94 xc functional with two different charges, −3 and +5, both of which have a closed-shell electronic structure. The charge effect is quite dramatic: whereas with a charge of −3 a clear-cut plasmon is observed, with a charge of +5 the sharp plasmonic peak disappears and a broader structure whose maximum is red-shifted by about 0.7 eV is obtained. A very similar and equally strong effect in which the plasmon is quenched was observed in the icosahedral silver cage,[52] $[Ag_{92}]^{2+}$, when passing from LB94 to the LDA xc functional.[24] This behavior indicates that the plasmon is not yet robust and that a change in the number of electrons and therefore in the electronic structure is enough to quench it; this effect is expected to be larger for smaller clusters, where quantum size effects are more pronounced. Nevertheless, it should be noted that a change of eight electrons is significant for a cluster containing only 55 atoms. The effect of the xc functional on $[Ag_{55}]^{5+}$ is quite modest (central panel), as is the charge effect using the PBE functional (lower panel). In the upper panel of Figure 6, we considered the effect of the basis set in the case of the PBE functional. Only rather modest differences are evident on going from the DZ to TZ2P set, with the most important one being the shift in the maximum of about 0.2 eV to lower energy, as expected because of the greater variational freedom assured by the larger basis set on the excited-state wave function. Finally, in the lower panel of Figure 6, the spectra calculated with QE and CP2K have been reported together with that calculated from complex polarizability. The agreement between QE and CP2K is excellent, but the complex polarizability approach slightly overestimates the position of the peak at around 3.9 eV. This disagreement is likely an effect of the basis set: as discussed above, a basis set enlargement tends to decrease the peak energy (upper panel), thus going in the direction of the QE and CP2K results.

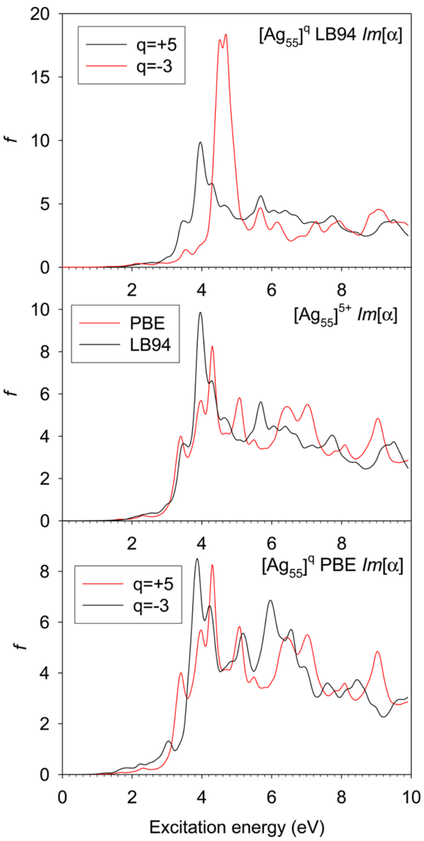

Figure 5. Photoabsorption profiles of $[Ag_{55}]^q$ calculated by complex polarizability TDDFT DZ and imaginary broadening ω_i = 0.15 eV. The charge and xc are shown in the insets.

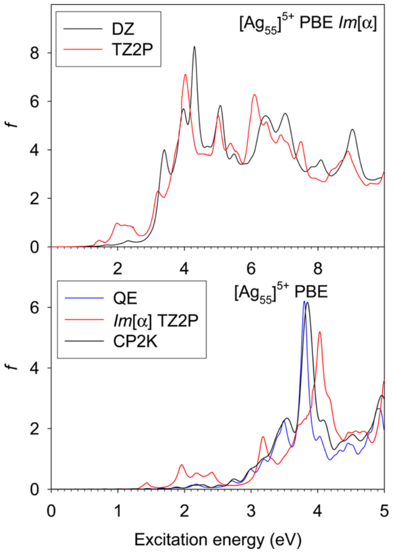

Figure 6. Photoabsorption profiles of $[Ag_{55}]^{5+}$ calculated by TDDFT PBE. Upper panel: complex polarizability with imaginary broadening ω_i = 0.15 eV. Lower panel: QE, CP2K, and complex polarizability with imaginary broadening ω_i = 0.075 eV. Basis sets and methods are shown in the insets.

In Figure S3, we have also compared the present complex polarizability algorithm with ADF results for both $[Ag_{55}]^{3-}$ and $[Ag_{147}]^{-}$, and the discrepancies are within the limits already found in the previous work.[13] In $[Ag_{147}]^{-}$, ADF gives a plasmon resonance that is a little bit too wide with respect to the complex polarizability method, which is likely due to the presence of two strong individual lines in the discrete spectrum, and tiny variations in the energy difference between the two lines are enough to cause a change to the plasmon shape.

4.5. Analysis of Photoabsorption for $[Au_{55}]^q$. In Figure 7, we have performed the same analysis as that concerning the charge and the xc effects for $[Au_{55}]^q$ clusters. At variance with respect to silver, the effects for $[Au_{55}]^q$ are not relevant: the general shape of the profiles does not change qualitatively if the charge or the xc functional is varied. It is curious that for both LB94 and PBE the change in the charge state from −3 to +5 causes a red shift at low energy and a blue shift for energies above 6 eV, so the charge effect cannot be simplified as a rigid translation on the energy scale.

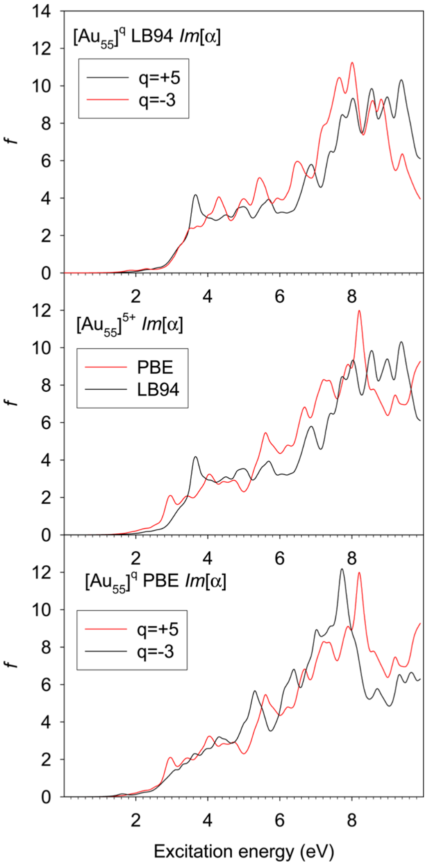

Figure 7. Photoabsorption profiles of $[Au_{55}]^q$ calculated by complex polarizability TDDFT DZ and imaginary broadening ω_i = 0.15 eV. The charge and XC are shown in the insets.

In Figure 8, the role of the basis set (upper panel) is considered. Going from DZ to TZ2P, a slight intensity decrease is observed for energies below 5 eV, whereas above 8 eV, the profiles look rather different, suggesting that the high-energy part of the spectrum is more demanding in terms of basis set requirements (as expected because we enter the continuum part of the spectrum). The comparison among the three methods (QE, CP2K, and complex polarizability) is fairly good: for the feature at 2.8 eV, the three methods are in excellent agreement with each other; only above 3.2 eV do some discrepancies appear, but they do not alter the qualitative shape of the profile. In conclusion, we can say that Ag_{55} is much more sensitive than Au_{55} to the charge, xc functional, and basis set as a result of the plasmon that is present only when the LB94 xc functional and charge −3 are employed. On the other hand, for Au_{55} the plasmon is not yet present in full; therefore, the spectral differences are consequences of subtle modifications of the electronic structure.

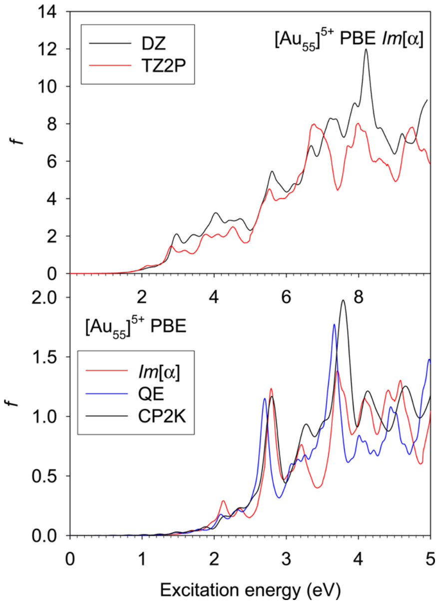

Figure 8. Photoabsorption profiles of $[Au_{55}]^{5+}$ calculated by TDDFT PBE. Upper panel: complex polarizability with imaginary broadening ω_i = 0.15 eV. Lower panel: QE, CP2K, and complex polarizability with imaginary broadening ω_i = 0.075 eV. Basis sets and methods are shown in the insets.

In Figure S3, we have also compared the present complex polarizability algorithm with ADF results for both $[Au_{55}]^{3-}$ and $[Au_{147}]^{-}$, and the discrepancies are within the limits already found in the previous work.[13] In this case, it is apparent that for the basis set employed in the ADF code it is very hard to describe the high-energy part of the spectrum, which is properly described only up to 4.0 and 3.5 eV for $[Au_{55}]^{3-}$ and $[Au_{147}]^{-}$ respectively.

Finally, we compare the performances in terms of computational efforts among the three methods (CP2K, QE, and complex polarizability) for $[Au_{55}]^{3-}$. CP2K was run on a cluster employing 96-core Dual Intel Haswell E5-2670 CPUs (2.3 Ghz) and needed 5 h 54 min (elapsed time) to complete all calculations. The QE was run on a Linux Infiniband cluster employing 192-core Intel Haswell (2.4 GHz) processors and needed 4 h 55 min. The complex polarizability program was run on a HP Proliant ML350 gen9 server employing 10-core Intel Xeon E5-2650-V3 (2.3Ghz) processors and needed 4 h 38 min. Of course, for an accurate timing comparison the same computer and the same core number should have been employed. However, if we assume that CPU time is the elapsed time multiplied by the core numbers and that it is corrected for the clock frequency, then we find that the computational efforts for CP2K, QE, and complex polarizability are proportional to 12:21:1, respectively. Although these numbers should be taken with caution, we can conclude by saying that the present complex polarizability algorithm can be even 1 order of magnitude more efficient with respect to other codes such as CP2K and QE for metal clusters containing up to 55 atoms. Such a comparison should not be extrapolated to a larger cluster size that deserves more specific analysis.

5. CONCLUSIONS

In this work, we have applied a recently developed new TDDFT algorithm[13] to a series of closed-shell icosahedral Ag and Au clusters, containing from 13 to 309 atoms. The photoabsorption spectrum is extracted from the imaginary part of the complex dynamical polarizability, solving a nonhomogeneous linear system and avoiding the diagonalization of the Casida matrix, which represents a problematic step when too many eigenvalues need to be calculated to cover the large energy interval of interest. The new method has proven not only to be very efficient, but also very powerful in terms of the analysis of the excited-state wave function, which has been done by employing the 2D TCM scheme. For silver clusters, a very intense plasmon resonance has already been found for $[Ag_{55}]^{3-}$. When the cluster size increases, the feature gains intensity and is red-shifted, a behavior typical of plasmon resonances. The TCM analysis identified strong coupling among low-energy excited configurations with intraband sp → sp character, and d → sp interband excitations play a minor role. For gold clusters, the situation is quite different because we did not identify a single strong plasmon as in silver clusters but rather many features of comparable intensity. The TCM analysis revealed that only for the lowest-energy features can partial plasmonic behavior be singled out, with moderate coupling of low-energy excitations together with important interband d → sp excitations. As the energy increases, the coupling with low-energy excitations disappears and the features become pure interband d → sp excitations.

The analysis of the spectral features revealed that the photoabsorption in the $[Ag_{55}]^q$ cluster is very sensitive to the cluster charge and the choice of the xc functional and basis set. In particular, the strong plasmon calculated with the LB94 xc functional and $q = 3-$ is suppressed if the charge is changed to $q = 5+$ or if the PBE xc functional is employed. The PBE results obtained with the complex dynamical polarizability compare fairly well with those calculated by using real-time evolution or Lanczos approaches via the QE and CP2K codes. However, being so sensitive to physical and computational choices, when using localized basis functions attention needs to be paid to basis set completeness issues as shown by the fact that when using the new algorithm only a basis set enlargement from DZ to TZ2P produced nearly quantitative agreement with both QE and CP2K.

The same analysis for the $[Au_{55}]^q$ cluster shows that in this case the results are much less sensitive to the charge, xc functional, and basis set as a result of the marginal role played by plasmonic features that do not dominate the spectrum any longer. In this case, the match among the complex dynamical polarizability and the QE and CP2K methods is even better than for the silver homologue.

The efficiency of the complex dynamical polarizability method together with the power of the TCM analysis suggests that further applications to more complex and realistic systems, such as metal clusters protected by ligands and therefore with reduced symmetry, are feasible and should be able to make an important contribution to rationalize and clarify the many questions still existing in the field, triggering further technological applications.

■ AUTHOR INFORMATION

Corresponding Authors

*(M.S.) Tel: +39-040-5593949. E-mail: stener@univ.trieste.it.
*(A.F.) Tel: +39-050-3152447. E-mail: alessandro.fortunelli@cnr.it.
*(A.C.) Tel: +39-059-2055627. E-mail: arrigo.calzolari@nano.cnr.it.

Notes

The authors declare no competing financial interest.

■ ACKNOWLEDGMENTS

Computational support from the CINECA Supercomputing Centre within the ISCRA programme is gratefully acknowledged. Computational research by A.F. and L.S. was performed using PNNL Institutional Computing at Pacific Northwest National Laboratory. This work has been supported by MIUR (Programmi di Ricerca di Interesse Nazionale PRIN 2010−2010BNZ3F2_006 DESCARTES) of Italy.

■ REFERENCES

(1) Casida, M. E. In *Recent Advances in Density-Functional Methods*; Chong, D. P., Ed.; World Scientific: Singapore, 1995; p 155.

(2) Baerends, E. J.; Ellis, D. E.; Ros, P. Self-consistent molecular Hartree—Fock—Slater calculations I. The computational procedure. *Chem. Phys.* **1973**, *2*, 41−51.

(3) Fonseca Guerra, C.; Snijders, J. G.; te Velde, G.; Baerends, E. J. Towards an order-N DFT method. *Theor. Chem. Acc.* **1998**, *99*, 391−403.

(4) van Gisbergen, S. J. A.; Snijders, J. G.; Baerends, E. J. Implementation of time-dependent density functional response equations. *Comput. Phys. Commun.* **1999**, *118*, 119−138.

(5) Yabana, K.; Bertsch, G. F. Time-dependent local-density approximation in real time. *Phys. Rev. B: Condens. Matter Mater. Phys.* **1996**, *54*, 4484−4487.

(6) Walker, B.; Saitta, A. M.; Gebauer, R.; Baroni, S. Efficient Approach to Time-Dependent Density-Functional Perturbation Theory for Optical Spectroscopy. *Phys. Rev. Lett.* **2006**, *96*, 113001.

(7) Grimme, S. A simplified Tamm-Dancoff density functional approach for the electronic excitation spectra of very large molecules. *J. Chem. Phys.* **2013**, *138*, 244104.

(8) Bannwarth, C.; Grimme, S. A simplified time-dependent density functional theory approach for electronic ultraviolet and circular dichroism spectra of very large molecules. *Comput. Theor. Chem.* **2014**, *1040−1041*, 45−53.

(9) Zuehlsdorff, T. J.; Hine, N. D. M.; Spencer, J. S.; Harrison, N. M.; Riley, D. J.; Haynes, P. D. Linear-scaling time-dependent density-functional theory in the linear response formalism. *J. Chem. Phys.* **2013**, *139*, 064104.

(10) Noda, M.; Ishimura, K.; Nobusada, K.; Yabana, K.; Boku, T. Massively-parallel electron dynamics calculations in real-time and real-space: Toward applications to nanostructures of more than ten-nanometers in size. *J. Comput. Phys.* **2014**, *265*, 145−155.

(11) Tussupbayev, S.; Govind, N.; Lopata, K.; Cramer, C. J. Comparison of real-time and linear-response time-dependent density functional theories for molecular chromophores ranging from sparse to high densities of states. *J. Chem. Theory Comput.* **2015**, *11*, 1102−1109.

(12) Li, Z.; Liu, W. Spin-adapted open-shell time-dependent density functional theory. III. An even better and simpler formulation. *J. Chem. Phys.* **2011**, *135*, 194106.

(13) Baseggio, O.; Fronzoni, G.; Stener, M. A new time dependent density functional algorithm for large systems and plasmons in metal clusters. *J. Chem. Phys.* **2015**, *143*, 024106.

(14) Kreibig, K.; Vollmer, M. *Optical Properties of Metal Clusters*; Springer: New York, 1995.

(15) Zhang, C.; Noguez, J. Z. Plasmonic Optical Properties and Applications of Metal Nanostructures. *Plasmonics* **2008**, *3*, 127−150.

(16) Burda, C.; Chen, X.; Narayanan, R.; El-Sayed, M. A. Chemistry and Properties of Nanocrystals of Different Shapes. *Chem. Rev.* **2005**, *105*, 1025−1102.

(17) Lippert, G.; Hutter, J.; Parrinello, M. The Gaussian and augmented-plane-wave density functional method for ab initio molecular dynamics simulations. *Theor. Chem. Acc.* **1999**, *103*, 124−140.

(18) Giannozzi, P.; Baroni, S.; Bonini, N.; Calandra, M.; Car, R.; Cavazzoni, C.; Ceresoli, D.; Chiarotti, G. L.; Cococcioni, M.; Dabo, I.; et al. QUANTUM ESPRESSO: a modular and open-source software project for quantum simulations of materials. *J. Phys.: Condens. Matter* **2009**, *21*, 395502.

(19) Jensen, L.; Autschbach, J.; Schatz, G. C. Finite lifetime effects on the polarizability within time-dependent density-functional theory. *J. Chem. Phys.* **2005**, *122*, 224115.

(20) Gross, E. K. U.; Kohn, W. Time-dependent density-functional theory. *Adv. Quantum Chem.* **1990**, *21*, 255−291.

(21) Malcioglu, O.; Gebauer, R.; Rocca, D.; Baroni, S. turboTDDFT − A code for the simulation of molecular spectra using the Liouville−Lanczos approach to time-dependent density-functional perturbation theory. *Comput. Phys. Commun.* **2011**, *182*, 1744−1754.

(22) Van Leeuwen, R.; Baerends, E. J. Exchange-correlation potential with correct asymptotic behavior. *Phys. Rev. A: At., Mol., Opt. Phys.* **1994**, *49*, 2421−2431.

(23) Perdew, J. P.; Burke, K.; Ernzerhof, M. Generalized Gradient Approximation Made Simple. *Phys. Rev. Lett.* **1996**, *77*, 3865−3868.

(24) Vosko, S. H.; Wilk, L.; Nusair, M. Accurate spin-dependent electron liquid correlation energies for local spin density calculations: a critical analysis. *Can. J. Phys.* **1980**, *58*, 1200−1211.

(25) van Lenthe, E.; Baerends, E. J.; Snijders, J. G. Relativistic regular two-component Hamiltonians. *J. Chem. Phys.* **1993**, *99*, 4597−4610.

(26) VandeVondele, J.; Hutter, J. Gaussian basis sets for accurate calculations on molecular systems in gas and condensed phases. *J. Chem. Phys.* **2007**, *127*, 114105.

(27) Hartwigsen, C.; Goedecker, S.; Hutter, J. Relativistic separable dual-space Gaussian pseudopotentials from H to Rn. *Phys. Rev. B: Condens. Matter Mater. Phys.* **1998**, *58*, 3641−3662.

(28) Vanderbilt, D. Soft self-consistent pseudopotentials in a generalized eigenvalue formalism. *Phys. Rev. B: Condens. Matter Mater. Phys.* **1990**, *41*, R7892−R7895.

(29) Martyna, J. G.; Tuckerman, M. E. A reciprocal space based method for treating long range interactions in ab initio and force-field-based calculations in clusters. *J. Chem. Phys.* **1999**, *110*, 2810−2821.

(30) Piccini, G. M.; Havenith, R. W. A.; Broer, R.; Stener, M. Gold Nanowires: A Time-Dependent Density Functional Assessment of Plasmonic Behavior. *J. Phys. Chem. C* **2013**, *117*, 17196−17204.

(31) Johnson, H. E.; Aikens, C. A. Electronic Structure and. TDDFT Optical Absorption Spectra of Silver Nanorods. *J. Phys. Chem. A* **2009**, *113*, 4445−4450.

(32) Aikens, C. M.; Li, S.; Schatz, G. C. From Discrete Electronic States to Plasmons: TDDFT Optical Absorption Properties of Ag_n (n = 10, 20, 35, 56, 84, 120) Tetrahedral Clusters. *J. Phys. Chem. C* **2008**, *112*, 11272−11279.

(33) Guidez, E. B.; Aikens, C. M. Theoretical Analysis of the Optical Excitation Spectra of Silver and Gold Nanowires. *Nanoscale* **2012**, *4*, 4190−4198.

(34) Guidez, E. B.; Aikens, C. M. Diameter Dependence of the Excitation Spectra of Silver and Gold Nanorods. *J. Phys. Chem. C* **2013**, *117*, 12325−12336.

(35) Rabilloud, F. Description of plasmon-like band in silver clusters: The importance of the long-range Hartree-Fock exchange in time-dependent density-functional theory simulations. *J. Chem. Phys.* **2014**, *141*, 144302.

(36) Harb, M.; Rabilloud, F.; Simon, D.; Rydlo, A.; Lecoultre, S.; Conus, F.; Rodrigues, V.; Felix, C. Optical absorption of small silver clusters: Ag_n, (n = 4−22). *J. Chem. Phys.* **2008**, *129*, 194108.

(37) Weissker, H-Ch; Mottet, C. Optical properties of pure and core-shell noble-metal nanoclusters from TDDFT: The influence of the atomic structure. *Phys. Rev. B: Condens. Matter Mater. Phys.* **2011**, *84*, 165443.

(38) Lopez-Lozano, X.; Barron, H.; Mottet, C.; Weissker, H.-C. Aspect-ratio- and size-dependent emergence of the surface-plasmon resonance in gold nanorods − an ab initio TDDFT study. *Phys. Chem. Chem. Phys.* **2014**, *16*, 1820−1823.

(39) Weissker, H.-C.; Lopez-Lozano, X. Surface plasmons in quantum-sized noble-metal clusters: TDDFT quantum calculations and the classical picture of charge oscillations. *Phys. Chem. Chem. Phys.* **2015**, *17*, 28379−28386.

(40) Bae, G. T.; Aikens, C. M. Time-Dependent Density Functional Theory Studies of Optical Properties of Ag Nanoparticles: Octahedra, Truncated Octahedra, and Icosahedra. *J. Phys. Chem. C* **2012**, *116*, 10356−10367.

(41) Kuisma, M.; Sakko, A.; Rossi, T. P.; Larsen, A. H.; Enkovaara, J.; Lehtovaara, L.; Rantala, T. T. Localized surface plasmon resonance in silver nanoparticles: Atomistic first-principles time-dependent density-functional theory calculations. *Phys. Rev. B: Condens. Matter Mater. Phys.* **2015**, *91*, 115431.

(42) Bae, G. T.; Aikens, C. M. Time-Dependent Density Functional Theory Studies of Optical Properties of Au Nanoparticles: Octahedra, Truncated Octahedra, and Icosahedra. *J. Phys. Chem. C* **2015**, *119*, 23127−23137.

(43) Iida, K.; Noda, M.; Ishimura, K.; Nobusada, K. First-Principles Computational Visualization of Localized Surface Plasmon Resonance in Gold Nanoclusters. *J. Phys. Chem. A* **2014**, *118*, 11317−11322.

(44) Ma, J.; Wang, Z.; Wang, L.-W. Interplay between plasmon and single-particle excitations in a metal nanocluster. *Nat. Commun.* **2015**, *6*, 10107.

(45) Malola, S.; Lehtovaara, L.; Enkovaara, J.; Häkkinen, H. Birth of the Localized Surface Plasmon Resonance in Monolayer-Protected Gold Nanoclusters. *ACS Nano* **2013**, *7*, 10263−10270.

(46) Durante, N.; Fortunelli, A.; Broyer, M.; Stener, M. Optical Properties of Au Nanoclusters from TD-DFT Calculations. *J. Phys. Chem. C* **2011**, *115*, 6277−6282.

(47) Liebsch, A. Surface-plasmon dispersion and size dependence of Mie resonance: Silver versus simple metals. *Phys. Rev. B: Condens. Matter Mater. Phys.* **1993**, *48*, 11317−11328.

(48) Kuisma, M.; Ojanen, J.; Rantala, T. T. Kohn-Sham potential with discontinuity for band gap materials. *Phys. Rev. B: Condens. Matter Mater. Phys.* **2010**, *82*, 115106.

(49) Gritsenko, O.; van Leeuwen, R.; van Lenthe, E.; Baerends, E. J. Self-consistent approximation to the Kohn-Sham exchange potential. *Phys. Rev. A: At., Mol., Opt. Phys.* **1995**, *51*, 1944−1954.

(50) Bernadotte, S.; Evers, F.; Jacob, C. R. Plasmons in Molecules. *J. Phys. Chem. C* **2013**, *117*, 1863−1878.

(51) Guidez, E. B.; Aikens, C. M. Quantum mechanical origin of the plasmon: from molecular systems to nanoparticles. *Nanoscale* **2014**, *6*, 11512−11527.

(52) Barcaro, G.; Sementa, L.; Fortunelli, A.; Stener, M. Optical Properties of Silver Nanoshells from Time-Dependent Density Functional Theory Calculations. *J. Phys. Chem. C* **2014**, *118*, 12450−12458.